Microstructure-dependent rate theory model of defect segregation and phase stability in irradiated polycrystalline $LiAlO_2$

Shenyang Hu[a*], Yulan Li[a], Shunli Shang[b], Zi-Kui Liu[b], Douglas Burkes[a], and David J. Senor[a]

[a] *Pacific Northwest National Laboratory, PO Box 999, Richland, WA 99352, USA.*

[b] *Department of Materials Science and Engineering, The Pennsylvania State University, University Park, Pennsylvania 16802*

[*] *Shenyang.hu@pnnl.gov*

Abstract

Gamma lithium aluminate ($LiAlO_2$) is a breeder material for tritium and is one of key components in a tritium-producing burnable absorber rod (TPBAR). Dissolution and precipitation of second phases such as $LiAl_5O_8$ and voids are observed in irradiated $LiAlO_2$. Such microstructure changes cause the degradation of thermomechanical properties of $LiAlO_2$ and affect tritium retention and release kinetics, and hence, the TPBAR performance. In this work, a microstructure-dependent model of radiation-induced segregation (RIS) has been developed for investigating the accumulation of species and phase stability in polycrystalline $LiAlO_2$ structures under irradiation. Three sublattices (i.e., $[Li, Al, V]^{I}$ $[O, V_o]^{II}$ $[Li_i, Al_i, O_i, V_i]^{III}$), and concentrations of six diffusive species (i.e., Li; vacancy of Li or Al at $[Li, Al, V]^{I}$ sublattice, O vacancy at $[O, V_o]^{II}$ sublattice, and Li, Al and O interstitials at $[Li_i, Al_i, O_i, V_i]^{III}$ interstitial sublattices; are used to describe spatial and temporal distributions of defects and chemistry. Microstructure-dependent thermodynamic and kinetic properties including the generation, reaction, and chemical potentials of defects and defect mobility are taken into account in the model. The parametric studies demonstrated the capability of the developed RIS model to assess the effect of thermodynamic and kinetic properties of defects on the segregation and depletion of species in polycrystalline structures and to explain the phase stability observed in irradiated $LiAlO_2$ samples. The developed RIS model will be extended to study the precipitation of $LiAl_5O_8$ and voids and tritium retention by integrating the phase-field method.

Keywords: Microstructure; Rate Theory; Radiation-induced segregation; $LiAlO_2$

1.0 **Introduction**

Microstructure images of irradiated $LiAlO_2$ clearly show that radiation induces the formation and growth of the second phase particle $LiAl_5O_8$ and voids [1]. These microstructure changes affect not only the sink strength of defects and tritium, hence, their diffusion and accumulation kinetics, but also effective thermal conductivity and mechanical properties. Burkes et al. and Senor et al. proposed a framework of tritium-producing burnable absorber rod (TPBAR) performance that was based on the empirical correlations between microstructure and material properties [2, 3]. The tritium-release kinetics predicted by the performance model are largely underestimated compared with experimental results [2]. To improve the predictive capability of such a performance model, one needs the knowledge of evolution kinetics of $LiAl_5O_8$ and voids, and the development of more accurate correlations between evolving microstructures and thermo-mechanical properties in radiated $LiAlO_2$.

The nuclear reaction between ^6Li in $LiAlO_2$ and a neutron [$^6Li + ^1n = ^4He$ (2.05MeV) + ^3T (2.75MeV)] produces high-energy fission fragments [He and tritium (T)]. The high energy fission fragments collide with atoms in the lattices and generate defects such as vacancies, interstitials, impurities, and their clusters. One nuclear reaction may generate thousands of Frenkel pairs [4]. As a consequence, vacancy and interstitial concentrations in irradiated $LiAlO_2$ might be a few orders of magnitude higher than their thermal equilibrium concentrations, which accelerate the diffusion of species. Furthermore, defects and species usually have different chemical potentials from their bulk chemical potentials at structural defects such as grain boundaries, free surfaces, and dislocations. The inhomogeneous chemical potentials in polycrystalline structures provide an additional diffusional driving force besides the concentration gradient driving force. The stability and growth kinetics of second-phase particle $LiAl_5O_8$ and voids depend on RIS of Li, Al, O, and vacancy. Therefore, the RIS model needs to take into account radiation-enhanced diffusion and inhomogeneous properties of species to capture the evolution of $LiAl_5O_8$ and voids.

Different methods such as rate theory [5-9], cluster dynamics [10-14], and phase-field approach [15-19] have been developed to investigate defect and microstructure evolutions in irradiated materials. Spatially distributed defects such as dislocations and grain boundaries are usually

described by sinks with effective sink strengths [9]. It is very efficient to predict the overall effect of microstructures (grain sizes, distributed dislocations and second phase particles) on defect concentration evolution. Cluster dynamics has the advantages in studying the temporal and spatial evolution of small defect clusters with interaction energies among defect clusters and defect mobility. However, nucleation and growth of a second-phase particle such as $LiAl_5O_8$ and voids relies on the phase stability depending on local species' concentrations and chemical free energy as well as the elastic interaction between diffusive defects and $LiAl_5O_8$ particles (there is an elastic field around $LiAl_5O_8$ particle due to the lattice mismatch between $LiAl_5O_8$ and $LiAlO_2$ matrix). For both rate theory and cluster dynamics approaches it is a challenge to capture the inhomogeneous evolution of defects that result from spatially distributed structural defects and temporally evolving particles. The phase field method is based on thermodynamic and kinetic properties of defects that can naturally describe inhomogeneous chemical potentials of defects associated with distributed structural defects, nonuniform chemistry, and long-range interactions. In our recent work [20] we developed a microstructure-dependent rate theory of RIS model in a binary AB alloy by integrating rate theory and the concept of defect chemical potential used in phase-field models.

In this work, we extended the RIS model in AB alloys to polycrystalline $LiAlO_2$ for studying the effect of thermodynamic and kinetic properties of defects on the segregation of Li, Al, O and vacancy in polycrystalline $LiAlO_2$ and understanding the physics behind the phase stability and microstructure evolution observed in radiated $LiAlO_2$.

2.0 Microstructure-dependent rate theory model

2.1 Description of chemistry and defects

The high-energy fission fragments associated with the nuclear reaction between ^6Li in $LiAlO_2$ and a neutron [$^6Li + ^1n = ^4He$ (2.05MeV) + ^3T (2.75MeV)] collide with host atoms in $LiAlO_2$ and generate defects such as vacancies, interstitials, impurities, and their clusters. The molecular dynamics simulations of cascades under 5keV primary knock-on atoms (PKA) in $LiAlO_2$ show that interstitials of Li, Al, and O; antisite defects of Li and Al at Li and Al lattices; and vacancies at Li, Al, and O lattices are generated [7]. The cascade generates 13 Frenkel pairs of Li

interstitials and vacancies that are about two times the Frenkel pairs of Al interstitials and vacancies; 3 Li antisites at Al lattices that are similar to those of Al antisites at Li lattices; and 13 Frenkel pairs of O vacancies and interstitials. The results clearly show that the defect generation rates of species (Li, Al and O) are quite different in $LiAlO_2$. Defect generation rates are not proportional to the local concentration of species, which is often assumed in the conventional rate theory. Lee et al. [21] calculated the formation energies of defects in $LiAlO_2$. The results showed that the stable defects may have charges, depending on the local fermi level or local electron structure. The different charged defects might tightly bind or strongly repel that affect the formation of antisite defects such as Al antisite at Li lattice and Al antisite at Li lattice, and their mobility, which is similar to the interaction between interstitials and undersize solutes [8]. Therefore, although the generation rate of Li antisites is similar to that of Al antisites under energy particle cascade, the dissociation reaction rate of Li antisites may be different from that of Al antisites due to different binding energies. Considering the facts above, Li and Al interstitials should be described by independent concentration fields.

$LiAlO_2$ has a tetragonal structure with space group $P4_12_12$ (No. 92), where the metals Li and Al occupy the Wyckoff sites 4a and 4a, respectively, and oxygen occupies the Wyckoff site 8b. By assuming the possible interstitial atoms (Li_i, Al_i, O_i, and vacancy V_i) occupy another Wyckoff site 8b, the defects and chemistry in radiated $LiAlO_2$ can be described by a three-sublattice model,

$$[Li, Al, V]^{I} [O, V_o]^{II} [Li_i, Al_i, O_i, V_i]^{III} \quad (1)$$

with the sublattice fraction ratios of 1:1:1, corresponding to the metal sublattice, the oxygen sublattice, and the interstitial sublattice, respectively. Six independent species (i.e., Li^I and vacancy V^I on the metal sublattice I; V_O^{II} on the O sublattice II; and Li_i^{III}, Al_i^{III}, and O_i^{III} on the interstitial sublattice III) can be used to describe the spatial and temporal distributions of defects and chemistry in $LiAlO_2$. In the present work, we define that the species (i.e., the component) concentration c_i^t (i = Li, Al, O, or V) equals to its site fraction y_i^t in each sublattice t (= I, II, or II); see Eq. (1).

2.2 Chemical potentials

The Gibbs energy of a general sublattice model G_{mf} can be written as follows in per mole of formula (mf) [22, 23]:

$$G_{mf} = \sum_{em}(\prod_t c_i^t \, G_{em}^0) + RT \sum_t a^t \sum_i c_i^t \ln y_i^t + {}^E G_{mf} \quad (2)$$

where R is the molar gas constant and T the absolute temperature. G_{em}^0 is the Gibbs energy of an endmember (em) with only one component in each sublattice t (there are 24 endmembers in the present three-sublattice model of Eq. (1)). G_{em}^0 is usually a function with respect to chemical potentials of components i (μ_i^0 with i = Li, Al, O, and V) and its Gibbs energy of formation. y_i^t is the site fraction of component i in sublattice t. ${}^E G_{mf}$ is the excess Gibbs energy of formation. By merging the Gibbs energies of formation of endmembers and the ${}^E G_{mf}$ into binding energies, merging activity coefficient γ_i into configurational entropy, and using the relationship $c_i^t = y_i^t$, Eq. (2) can be expressed as,

$$G = \sum_{m=Li,Al,V} [c_m^I \mu_m^0 + RT(c_m^I \ln(\gamma_m^I c_m^I))] + \sum_{m=O,V} [c_m^{II} \mu_m^0 + RT(c_m^{II} \ln(\gamma_m^{II} c_m^{II}))]$$
$$+ \sum_{m=Li,Al,O} [c_m^{III} \mu_m^0 + RT(c_m^{III} \ln(\gamma_m^{III} c_m^{III}))] + \sum_j \left[\sum_i c_i c_j z_{ij} E_{ij}^{binding}\right] \quad (3)$$

where i represents the components in the sublattices I and II, and j the components in the sublattice III as shown in Eq. (1); introducing the binding energies ($E_{ij}^{binding}$) between components i and j.

Chemical potentials of species at structural defects such as grain boundaries (GBs), interfaces, and surfaces are usually different from those inside the grains. The microstructure and/or spatial dependent chemical potential in polycrystalline $LiAlO_2$ structure cause an additional diffusion driving force that affects the fluxes of defects and species, hence, their segregation, depletion, and phase stability. To capture the effect of grain boundaries on RIS, we extended the conventional rate theory to a microstructure-dependent rate theory model. In the model one set of order parameters $\eta_m (m = 1,2,\cdots,m_0)$ are used to describe the grain orientations in the polycrystalline structure where m_0 is the total number of grain orientations in the simulation cell. The order parameter η_m, which is obtained from phase-field modeling of grain growth, has the values of 1 inside the grain m, and 0 outside of the grain m, and continuously varies from 1 to 0 across the grain boundary. We defined a shape function with the order parameters as $f(\eta) =$

$2.0(1-\sum_{m=1}^{m_0}(\eta_m)^2)$ that varies smoothly from 0 inside the grains to 1.0 at the center of GBs. The thermodynamic properties of the GBs are expected to closely correlate with the atomic density and composition. Van der Waals [24] showed that the energy of an interface can be described as a function of mass density and its variations within the interface region. Very recently, Kamachali et al. [25] proposed a density-based thermodynamic model of grain boundaries. The Gibbs free energy of GBs is described by bulk free energy, atomic density, gradient coefficient of atomic density. A Gaussian function is used to describe the atomic density change across the GB that evolves with composition. Atomic simulations [25] in alpha Fe showed that the atomic density of a GB with high symmetry has the Gaussian distribution. The atomic density of a GB can be approximately described by a shape function $\rho_0 + \rho^{GB} f(\eta)$ that is equal to ρ_0 inside the grain and smoothly varies to $\rho_0 + \rho^{GB}$ at the center of the GB. ρ_0 is the density of a perfect crystal while ρ^{GB} is the difference of atomic density between those inside a grain and on the grain boundary due to free volume at the center of the grain boundary. Similarly, other spatially dependent thermodynamic properties of defect di such as chemical potential and diffusivity of species can also be described as $\Phi_{di} = \Phi_{0di}(c_m, T) + \Phi_{di}^{GB}(c_m, T)f(\eta)$. $\Phi_{0di}(c_m, T)$ is the property of defect di inside a grain, and $\Phi_{di}^{GB}(c_m, T)f(\eta)$ is the difference of the property of defect di on the GB from that inside the grain. di denotes any of the defects, i.e., $di = Ai, Bi, V, A, Oi,$ or OV. Therefore, the microstructure-dependent chemical potential of species j can be written as

$$\mu_j = \mu_j^M + \mu_j^{GB}(c_m, T)f(\eta) \tag{4}$$

where μ_j^M is the bulk chemical potential of species *j*, μ_j^{GB} is the difference of chemical potential of species *j* between inside a grain and at the center of grain boundaries. In principle, μ_j^{GB} can be determined by $\mu_i\left(c_i^{eq}|_m\right) = \mu_i\left(c_i^{eq}|_{gb}\right)$. $c_i^{eq}|_m$ and $c_i^{eq}|_{gb}$ are the thermal equilibrium concentration of defect *i* inside grains and at grain boundaries, respectively. The diffusivity inhomogeneity can be described by a similar expression as the Eq. (4). In $LiAlO_2$, all the defects are charged. For example, Li and Al interstitials and O vacancy have positive charges while Li and Al vacancies and O interstitial have negative charges. Any accumulation of charged defects causes an electric potential (an electric potential ϕ), which affects the migration of the charged defects. Adding the electric potential, the electrochemical potential is given by

$$\mu_j = \mu_j^M + \mu_j^{GB}(c_m, T)f(\eta) + q_j\phi \tag{5}$$

where q_j is the valence of defect j, and E is the electric field ($E = -\nabla\phi$). The electric potential ϕ satisfies the Poisson's equation. However, in this work, we assume that all species are neutral to simplify the model. It will be straight forward to include the charge effect in the model if relative thermodynamic and kinetic properties of defects are available in future.

2.3 Microstructure-dependent rate theory

Recently, we developed a microstructure-dependent rate theory model of RIS to take into account grain morphology and inhomogeneous thermodynamic and kinetic properties of defects in polycrystalline AB alloys [20]. A two sublattice model [A, B, V]^{I} [A_i, B_i, V_i]^{II} was used to describe the free energy of the system and defect evolution. In radiated $LiAlO_2$, the free energy of the system with defects can be described by a three sublattice model [Li, Al, V]^{I} [O, V_o]^{II} [Li_i, Al_i, O_i, V_i]^{III} in section 2.2. Here we extended the defect evolution equations in a two sublattice AB alloys to a three sublattice $LiAlO_2$.

To clearly and concisely present the extension from the two sublattice model to three sublattice model, we first provide the brief derivation of defect evolution equation in two sublattice model [20], then describe how to deduce the equations in three sublattice model [Li, Al, V]^{I} [O, V_o]^{II} [Li_i, Al_i, O_i, V_i]^{III} from the two sublattice model [A, B, V]^{I} [A_i, B_i, V_i]^{II}. Following to the rate theory, the evolution of chemical and defect concentrations in AB alloys with two sublattices is given by [8, 20]:

$$\frac{\partial c_\alpha(\boldsymbol{r},t)}{\partial t} = -\nabla \cdot J_\alpha(\boldsymbol{r},t), \qquad \alpha = A \text{ and } B \tag{6}$$

$$\frac{\partial c_d(\boldsymbol{r},t)}{\partial t} = -\nabla \cdot J_d(\boldsymbol{r},t) + \dot{g}_d + \dot{g}_d^S + \dot{g}_d^R, \quad d = V, Ai \text{ and } Bi, \tag{7}$$

where $J_\alpha(\boldsymbol{r},t)$ and $J_d(\boldsymbol{r},t)$ are the fluxes of atom α and defect d, respectively. $\dot{g}_d$, $\dot{g}_d^S$ and $\dot{g}_d^R$ is the generation rate, sink rate, and recombination rate of defect d, respectively. The atom and lattice conservation requires the fluxes should satisfy the following equations [20, 26]:

$$J_\alpha(\boldsymbol{r},t) = \sum_{d=V,Ai,Bi} J_\alpha^d(\boldsymbol{r},t) \tag{8}$$

$$J_d(\boldsymbol{r},t) = \sum_{\alpha=A,B} sign(d) J_\alpha^d(\boldsymbol{r},t) \tag{9}$$

where $J_\alpha^d(\boldsymbol{r},t)$ is the flux of atom α diffusing via defect d, $sign(d) = 1$ for $d = Ai$ or Bi and -1 for $d = V$. The fluxes of atoms and defects driven by chemical potential gradient can be approximately calculated by [26, 27],

$$J_\alpha^d(\boldsymbol{r},t) = -\sum_\beta \frac{L_{\alpha\beta}^d}{k_B T}\left(\nabla\mu_\beta + sign(d)\nabla\mu_d\right), \qquad \alpha,\beta = A \text{ and } B \tag{10}$$

where $L_{\alpha\beta}$ is the Onsager kinetic coefficient.

In polycrystalline structures the inhomogeneous chemical potential μ_α and μ_d are expressed as

$$\mu_\alpha(\boldsymbol{r},t) = \mu_\alpha^M + \mu_\alpha^{GB} f(\eta) \ = \mu_\alpha^0 + RTln(\gamma_\alpha c_\alpha) + \mu_\alpha^{GB} f(\eta), \tag{11}$$

$$\mu_d(\boldsymbol{r},t) = \mu_d^0 + RTln(c_d) + \mu_d^{GB} f(\eta). \tag{12}$$

If we assume that 1) the chemical potentials $\mu_\alpha^M, (\alpha = A \text{ and } B)$, satisfy the Gibbs-Duhem relationship $\sum_\alpha c_\alpha \nabla\mu_\alpha^M = 0$; 2) the defect concentration is low, i.e., $c_d << 1$; and 3) $L_{\alpha\beta}^d = 0$ for $\alpha \neq \beta$ the evolution Eqs. (6 -7) are simplified as

$$\frac{\partial c_{Ai}(\boldsymbol{r},t)}{\partial t} = \nabla\left[(d_{AA}^{Ai} c_{Ai}\phi\nabla c_A + d_{BB}^{Ai} c_{Ai}\phi\nabla c_B + (d_{AA}^{Ai} c_A + d_{BB}^{Ai} c_B)\nabla c_{Ai} + \kappa_{Ai}^{GB}\nabla f(\eta)\right] + \dot{g}_{Ai} + \dot{g}_{Ai}^S + \dot{g}_{Ai}^R, \tag{13}$$

$$\frac{\partial c_{Bi}(\boldsymbol{r},t)}{\partial t} = \nabla\left[(d_{AA}^{Bi} c_{Bi}\phi\nabla c_A + d_{BB}^{Bi} c_{Bi}\phi\nabla c_B + (d_{AA}^{Bi} c_A + d_{BB}^{Bi} c_B)\nabla c_{Bi} + \kappa_{Bi}^{GB}\nabla f(\eta)\right] + \dot{g}_{Bi} + \dot{g}_{Bi}^S + \dot{g}_{Bi}^R, \tag{14}$$

$$\frac{\partial c_V(\boldsymbol{r},t)}{\partial t} = \nabla[-d_{AA}^V c_V\phi\nabla c_A - d_{BB}^V c_V\phi\nabla c_B + (d_{AA}^V c_A + d_{BB}^V c_B)\nabla c_V + \kappa_V^{GB}\nabla f(\eta)] + \dot{g}_V + \dot{g}_V^S + \dot{g}_V^R, \tag{15}$$

$$\frac{\partial c_A(\boldsymbol{r},t)}{\partial t} = \nabla[\left(d_{AA}^V c_V + d_{AA}^{Ai} c_{Ai} + d_{AA}^{Bi} c_{Bi}\right)\phi\nabla c_A - d_{AA}^V c_A\nabla c_V + d_{AA}^{Ai} c_A\nabla c_{Ai} + d_{AA}^{Bi} c_A\nabla c_{Bi} + \kappa_A^{GB}\nabla f(\eta)], \tag{16}$$

where the normalized Onsager coefficient is defined as $d_{\alpha\beta}^d = L_{\alpha\beta}^d/(c_d c_\beta)$, and $\kappa_i^{GB}, (i = A, Ai, Bi, \text{and } V)$ are functions of defect concentrations and chemical potentials on grain boundaries. They are given by

$$\kappa_\alpha^{GB} = \sum_d \sum_\beta \frac{d_{\alpha\beta}^d c_d c_\beta}{k_B \mathrm{T}}\left[\mu_\beta^{GB} + sign(d)\mu_d^{GB}\right], \ \alpha = A \text{ and } B, \tag{17}$$

$$\kappa_d^{GB} = \sum_\alpha \sum_\beta \frac{d_{\alpha\beta}^d c_d c_\beta}{k_B \mathrm{T}}\left[\mathrm{sign(d)}\mu_\beta^{GB} + \mu_d^{GB}\right], \ d = V, Ai \text{ and } Bi. \tag{18}$$

Inside the grains where $f(\eta) = 0$, the evolution Eqs. (13-16) become to the rate equations (6-20) of ref. [8] with the assumption of $L_{AA}^d = L_{BB}^d$. The normalized Onsager coefficients $d_{\alpha\alpha}^d$ are the same as $d_{\alpha d}$ in the equations (6-20) of ref. [8] which is the diffusivity of atom α diffusing via the exchange with defect d on a given neighboring site. The diffusivity coefficient d_{ij} is given by

$$d_{ij} = \frac{1}{6}\lambda_{i,j}^2 f_{ij}\nu_{i,j} exp\left(\frac{-\Delta E_m^{ij}}{k_B T}\right) \tag{19}$$

where $\lambda_{i,j}$ is the jump distance when atom i and defect j exchange sites. f_{ij} is the correlation factor[28]. $\nu_{i,j}$ is the effective exchange-jump frequency of atom i - defect j pair, and ΔE_m^{ij} is the migration energy. In this work, $d_{\alpha\beta}^d = 0, \alpha \neq \beta$ and $d_{\alpha\alpha}^d = d_{\alpha d}$ are used.

If the notation A and B in Eqs. (6-18) are replaced by Li and Al, respectively, Eqs. (6-18) can be used to describe the concentration evolution of species in [Li, Al, V]^{I} and [Li_i, Al_i, V_i]^{III} sublattices. Similarly, if we assume $c_{Bi}(\boldsymbol{r}, t) = 0$, $c_A(\boldsymbol{r}, t) \cong 1$, and replace $c_{Ai}(\boldsymbol{r}, t)$ and $c_V(\boldsymbol{r}, t)$ by $c_{Oi}(\boldsymbol{r}, t)$ and $c_{ov}(\boldsymbol{r}, t)$, respectively, Eqs. (6-18) can be used to describe the concentration evolution of species in [O, V_o]^{II} and [O_i, V_i]^{III} sublattices. The interaction among species in three sublattices is described through the Gibb's free energy of Eq. (3) and defect kinetic properties.

3.0 Thermodynamic and kinetic properties and model parameters

The generation rate of defects $\dot{g}_d$ is assumed to be proportional to the alloy composition in the conventional rate theory. Since interstitials A and B are treated as individual variables in this work, accurate interstitial generation rates from MD cascade simulations can be used when they satisfy the relationship of $\dot{g}_V = \dot{g}_{Ai} + \dot{g}_{Bi}$. $\dot{g}_{Ai}$ and $\dot{g}_{Bi}$ are calculated by the equation of $\dot{g}_d = m_d \dot{K}$ where $\dot{K}$ is the dose rate and m_d is the production efficiency of defect d. For example, MD simulations show that $m_{Lii}/m_{Ali} = 4$ in $LiAlO_2$ [4]. The recombination rate of Frenkel defects $\dot{g}_d^R = -\alpha_{dV} c_d c_V, d = Ai$ and Bi. And $\dot{g}_V^R = -\sum_{d=Ai,Bi} \alpha_{dV} c_d c_V$. $\alpha_{dV} = z_{d,V}(D_d + D_V)/a^2$ is a rate constant, a is the lattice constant, and $z_{d,V}$ is the combination factor of vacancy and interstitial. In polycrystalline structures, the main sinks of defects are dislocations and grain boundaries. The sink rate of defects on distributed dislocations can be calculated by $\dot{g}_d^S = z_{d,dis} D_d \rho_{dis}(c_d - c_d^{eq})$, where $z_{d,dis}$ is the sink strength constant of defect d on dislocations. ρ_{dis} is the dislocation density. D_d is the diffusivity of defect d. c_d^{eq} is the thermal equilibrium concentration of defect d at dislocations. Grain boundaries can be described by an array of dislocations such as small angle grain boundaries[29] and/or can be described as plane defects with high defect concentrations as discussed in section 2.2. Defects (Ai, Bi, V) on grain boundaries may have different chemical potentials from those inside grains. Distributed dislocations on grain boundaries have elastic interaction with defects. Both the chemical potential and elastic interaction cause driving forces for defect diffusion. Conventional rate

theory assumes that defects on grain boundaries remain their thermal equilibrium concentrations. It should be a reasonable assumption after the system reaches a steady state. However, for a system far from equilibrium, the assumption might be inappropriate. For example, if solute interstitials have much higher diffusivity than that of vacancies, the solute interstitials may accumulate on grain boundaries and form supper saturated solution. The excess interstitials might be emitted back to interior grains. But it is also possible that the supper saturated solution or vacancies leads to the second phase formation or void formation on grain boundaries which are often observed in irradiated materials [30, 31]. In this work, the polycrystalline structure is naturally described in terms of inhomogeneous thermodynamic and kinetic properties. The sink of defects on grain boundaries is described by the local defect recombination $\dot{g}_d^R$ enhanced by high defect concentrations and high defect mobility. The assumption that defects on grain boundaries remain thermal equilibrium concentration is released.

To calculate the defect generation rate $\dot{g}_i^{cs}$, one needs to know the fission product (FP) yields and the kinetic energy distribution of the fission products. Greenwood [32] assessed the displacement per atom (dpa) rate in $LiAlO_2$, based on fission products. It is expressed as

$$dpa = 33.7XY \tag{20}$$

where X is the ^{6}Li enrichment and Y is the burnup. Thus, the dpa rate can be calculated as

$$\dot{K} = \frac{d(dap)}{dt} = 33.7X\frac{dY}{dt} \tag{21}$$

where dY/dt is the burnup rate. With the information of different defect generation in MD cascade simulations, one can estimate the defect generation rate with the assumption that the defect generation rate during the nuclear reaction is proportional to the defect generation rate in the cascade under 6keV PKA.

$$\dot{g}_i = \dot{\mathrm{K}}\frac{m_i}{\sum_j m_j} \tag{22}$$

where m_i is the number of defect *i* generated in the cascade under 6keV PKA.

Molecular dynamics (MD) simulations show that high-energy particle cascades in $LiAlO_2$ generate Frenkel pairs as well as antisite defects at [Li, Al] sublattice[4]. The binding energy between Li interstitial and Li vacancy is different from that between Li interstitial and Al vacancy, similarly for Al interstitials. A large binding energy between interstitial and antisite

vacancy causes antisite defect formation while a small binding energy might result in the association of antisite defects that affect their interstitial concentrations. For instance, if Al interstitial and Li vacancy have strong binding, more Al interstitials become Li antisite defect, hence, this exchange reduce Al interstitial and Li vacancy concentrations. To describe the effect of binding energy on defect reaction rate, an exchange term $\dot{g}_{dj}^{ex}$ is added into $\dot{g}_{d}^{R}$. The exchange rate between interstitial *d* and vacancy *j* is described as $\dot{g}_{dj}^{ex} = \beta_{dj}(D_d + D_j)\, c_d c_j$. For example, the exchange between Al *interstitial* and Li vacancy forms Al antisite and reduces Al interstitial and Li vacancy concentrations). β_{dj} is a coefficient that is positive for the antisite dissociation and negative for the antisite formation. Experiments show that Li on grain boundaries might quickly diffuse to the free surface of the $LiAlO_2$ pellet along grain boundaries. The sink rate depends on Li concentration on grain boundaries. In the simulations, the sink rate is defined as

$$\dot{S}_i = -S_0 \frac{d\left(c_i(r,t) - c_i^{eq}\right)}{dt}, \qquad if\ (c_i - c_i^{eq}) > 0$$
$$\dot{S}_i = 0, \qquad if\ \left(c_i - c_i^{eq}\right) \le 0 \tag{23}$$

where c_i^{eq} the equilibrium concentration of Li on grain boundaries in $LiAlO_2$, S_0 is a model parameter describing the percentage of defects that are absorbed by the grain boundary, and $f(\eta)$ define the location of the sink (grain boundaries). $S_0 = 1$ indicates that all defects diffusing to grain boundaries are absorbed by grain boundaries or all defects on grain boundaries quickly diffuse to the free surface along grain boundaries.

The normalized time $t^* = \frac{tD_0}{l_0^2}$, diffusivity $d_{ij}^* = \frac{d_{ij}}{D_0}$, length $\nabla^* = \nabla l_0$, and energy $\mu_j^* = \frac{\mu_j}{RT}$ are used to normalize Eq. (23). l_0 and $D_0 = \max\{d_{ij}\}$ are characteristic length, the largest diffusivity. R and T are the ideal gas constant and absolute temperature, respectively. Solving the equations, one has the spatial and temporal evolution of species concentration c_i. Atomistic simulations [4, 33-35] and experiments [36-38] show that Li migration energy is about 0.5eV to 1.26eV. The presence of defects associated with radiation damage and anisotropy of crystal structure strongly affects Li diffusion barrier [34]. No valid kinetic data such as migration barriers of Li, Al, and O interstitials and vacancy of Li, Al, and O exist in the literature. However, the fact that the Al interstitial has a larger atomic size and higher charges than that of Li interstitials suggests the diffusion barrier of Al should be much larger than that of Li. Table 1

lists the model parameters and thermodynamic and kinetic properties of species used in the simulations.

Table 1. Model parameters

Parameters	Name	Values
Lattice constant	a, c	$0.5169, 0.6268nm$
dpa rate	$\dot{K}$	3.0×10^{-5}
Defect	i	$1: Li_I, 2: Al_I, 3: V$ $4: Li, 5: O_V, 6: O_I$
Coefficient of defect generation rate	m_i $i = 1, 2, \cdots, 6$	$16, 8, 24, -0.0148, 16, 16$
Generation rates of different defects	$\dot{g}_i$	$(0.4, 0.2, 0.6, -0.00037, 0.4, 0.4)\dot{K}$
Characteristic length	l_0	$20\ nm$
Temperature	T	$500K$
Migration energy of Li in bulk	E_{Li}^m	0.5eV~1.26eV
Migration energy of Li via interstitial	ΔE_m^{ij}	0.8eV
Migration energy of Li via vacancy	ΔE_m^{ij}	1.2eV
Ratio of Al diffusivity via interstitial	d_{Bi}	$0.1d_{Ai}$
Ratio of Al diffusivity via vacancy	d_{Bv}	$0.01d_{Av}$
Migration energy of O via O interstitial	ΔE_m^{ij}	1.0eV
Migration energy of O via O vacancy	ΔE_m^{ij}	1.2eV
Pre-exponential factor in the diffusion coefficient via defect *i*	d_i^{eq}	$\alpha a^2 \nu c_i^{eq}(E_i^f)$
Equilibrium concentration of defect	$c_i^{eq}(E_i^f)$	$exp(-E_i^f/k_B T)$

Diffusion coefficient of defect *i* via defect *j*	d_{ij}	$d_j^{eq}\exp\left(-\Delta E_m^{ij}/k_B T\right)$
Jump distance	λ	Aa
Coefficient	A	$\frac{\sqrt{3}}{2} via\ V, \frac{1}{2}\ via\ I$
The number of nearest neighbors	z	8
Coefficient	α	$1/6zA^2$
Debye frequency	ν	$1.0 \times 10^{13}(1/s)$
Atomic volume	Ω	$1.04 \times 10^{-29}(m^3)$
Formation energy of defect Li, Al, O interstitials	E_i^f	5.99eV, 17.89eV, 1.67eV
Formation energy of defect Li, Al, O vacancies	E_i^f	1.91eV, 3.58eV, 6.26eV
Li absorption coefficient at grain boundary	S_0	0.2

4.0 **Results**

A phase field model of grain growth is used to generate polycrystalline structures. The grain boundaries are defined by a shape function $f(\eta) = 2(1. - \sum_{m=1}^{m_0}(\eta_m)^2)$ that has the value of 0 inside the grains and continuously varies to 1 at the center of the grain boundaries as shown in Fig. 1(b). The thermodynamic and kinetic properties of species on grain boundaries are defined by the shape function $f(\eta)$ and Δl as described in previous section.

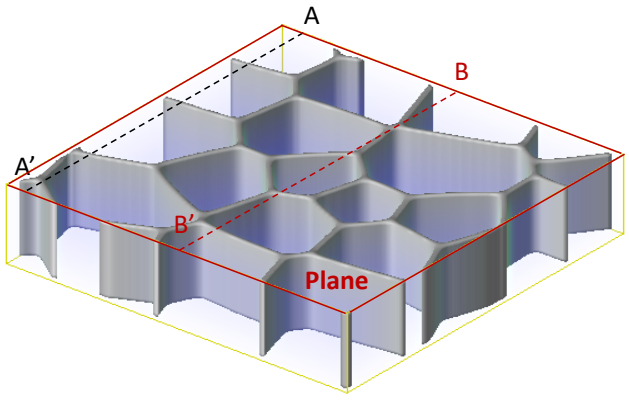

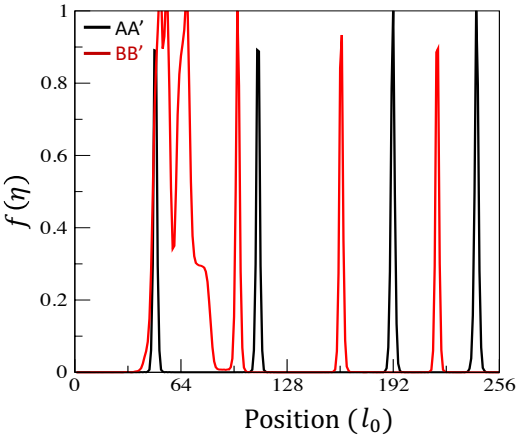

(a) (b)

Fig. 1. (a) the polycrystalline structure, and (b) the shape function along AA' and BB' lines shown in (a).

4.1 Effect of defect mobility and chemical potential on solute segregation in a surrogate binary A-B alloy

The developed model can be reduced to a RIS model of binary alloys [8] if the [O] sublattice is turned off, but with inhomogeneous thermodynamic and kinetics properties. We first simulated the effect of defect mobility and inhomogeneous solute chemical potential on solute segregation on grain boundaries in a surrogate binary A-B alloy. In the simulations, the concentration of solute A in AB alloys is 0.1. We assumed that 1) the grain boundary is a neutral sink for interstitials and vacancies; 2) dislocations are favored sinks for interstitials; and 3) diffusivity of defects on grain boundaries are the same as that of interior grains. The sink strength of dislocations can be calculated by $z_{id}\rho_{dis}$ for interstitials and $z_{vd}\rho_{dis}$ for vacancies [8]. $z_{id} = 1.25$, $z_{vd} = 1.0$, and dislocation density $\rho_{dis} = 1.0 \times 10^{14} m^2$ were used in the simulations. The partial diffusivity of solute A via vacancies is set to be much larger than that of solvent B, the partial diffusivity of A and B via interstitials is assumed to be the same, and they satisfy the condition: $\left(\frac{d_{Av}}{d_{Bv}} - \frac{d_{Ai}}{d_{Bi}}\right) = 99 > 0$. The dpa rate and other model parameters are listed in Table 1. The simulations were carried out in a polycrystalline structure with cylindrical grains as shown in Fig. 1(a). The same polycrystalline structure but with smaller grains in a simulation cell $128l_0 \times 128l_0 \times 32l_0$ ware used in the simulations. Fig. 2 shows the concentration distributions of vacancy, total interstitial, and solute A on the plane of $z = 32l_0$ at time $t^* = 140$. The colored bars show the concentration, while the white lines denote the grain boundaries. It is clear that on grain boundaries the vacancy and solute A have low concentrations while the interstitial has high concentration. Vacancy and interstitial concentrations of interior grains are uniform, depending on the grain size. For example, vacancy concentration inside large grains is higher than inside small grains. In addition, interstitial concentration of interior grains is much lower than that of vacancies. It can be explained that more interstitials sink to dislocations and grain boundaries because interstitials have larger sink strength at dislocations and much higher diffusivity than vacancies. The temporal evolutions of species on AA' line are plotted in Fig. 3. The interstitial concentrations inside grains and on grain boundaries decrease with time while vacancy

concentrations increase. The concentration of solute A on grain boundaries decreases with time. There is a flux of solute A from grain boundaries to the center of grains, which is in the opposite direction of vacancy and interstitial fluxes. In irradiated binary alloys, the vacancy flux and solute flux at steady state can be described as [8]

$$\Delta c_A = \frac{c_A c_B d_{Ai} d_{Bi}}{(d_{Bi} c_B D_A + d_{Ai} c_A D_B)} \left(\frac{d_{Av}}{d_{Bv}} - \frac{d_{Ai}}{d_{Bi}} \right) \Delta c_v \tag{24}$$

This indicates that when $\left(\frac{d_{Av}}{d_{Bv}} - \frac{d_{Ai}}{d_{Bi}} \right) > 0$, the concentration gradients of solute A and vacancy have the same sign. Considering the fact that 1) vacancies diffuse to grain boundaries down the concentration gradient, and 2) solute A should satisfy the mass conservation, the same sign of vacancy and solute A concentration gradients indicate that solute A diffuses uphill away from the grain boundaries. Therefore, the simulation results are in agreement with the prediction from the RIS model.

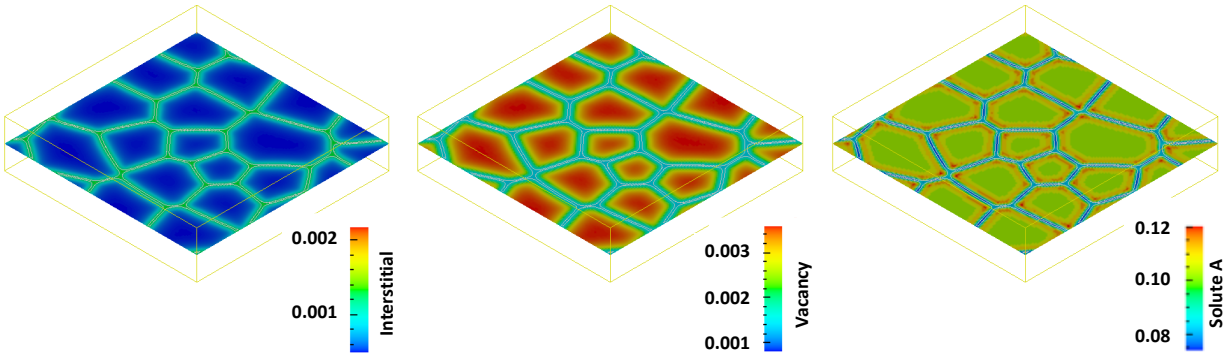

(a) (b) (c)

Fig. 2. Effect of defect mobility on defect segregation: (a) total interstitial, (b) vacancy, and (c) solute A.

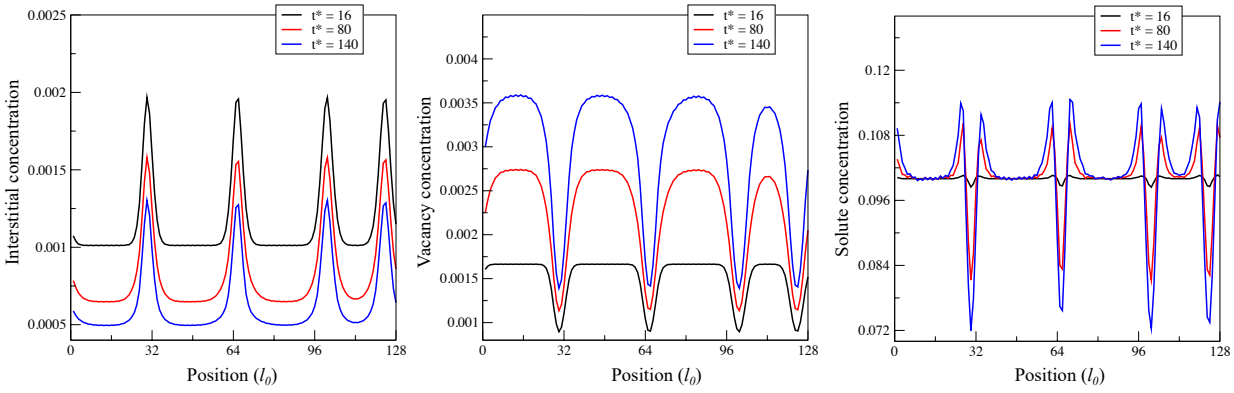

(a) (b) (c)

Fig. 3. Evolution of defect concentrations along the line AA' in Fig. 1 with a simulation cell $128l_0 \times 128l_0 \times 32l_0$, (a) Interstitial, (b) Vacancy, and (c) Solute A.

The chemical potential of solute A on grain boundaries could be different from that in bulk. Fig. 4 shows the effect of chemical potential of solute A on the segregation. $\mu_A^{GB} = -0.3eV$ means that the formation energy of solute A on grain boundaries is 0.3eV smaller than that in bulk. In this case, solute A segregates on grain boundaries as shown in Fig. 4(a). Increasing the chemical potential from $\mu_A^{GB} = -0.3eV \; to \; \mu_A^{GB} = 0.3eV$, solute A on grain boundaries changes from segregation to depletion as shown in Fig. 4. The results demonstrate that the solute segregation or depletion on grain boundaries not only depends on the kinetic properties of defects (relative diffusivity), but also the thermodynamic properties of solutes.

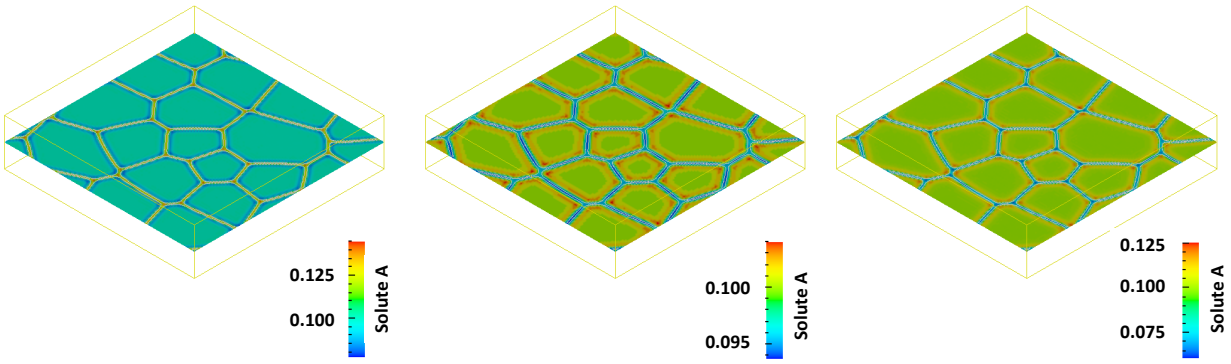

(a) (b) (c)

Fig. 4. Effect of chemical potential on solute segregation: (a) $\mu_A^{GB} = -0.3eV$, (b) $\mu_A^{GB} = 0.0eV$, (c) $\mu_A^{GB} = 0.3eV$.

4.2 Effect of thermodynamic and kinetic properties of defects on segregation in $LiAlO_2$

A number of thermodynamic and kinetic properties such as inhomogeneous chemical potential, binding energy, diffusivity, and reaction rate of defects may affect the RIS in $LiAlO_2$. It is very complicated to calculate the chemical potential of species on grain boundaries in $LiAlO_2$ for the following reasons: each species may have multiple energetically favored lattice sites, charge state may be different at different lattice sites, local chemistry affects the chemical potential, and all the effect factors change with time in irradiated $LiAlO_2$. The chemical potential of the species

also depends on the types of grain boundaries. For simplicity, the chemical potential of species *i* on grain boundaries is the same and is described by $\mu_i = \mu_i^M + \mu_i^{GB} f(\eta)$. μ_i^{GB} is the difference of chemical potential of species i on grain boundaries and interior grains. In reality, Li may diffuse to the $LiAlO_2$ pellet's surface through the grain boundaries. MD simulation [4] shows that the cascade (5keV) generates 13 Li interstitials and 3 Li antisites. The Li antisites may associate to Li interstitial and Al vacancy, or the Li interstitial may combine with the Al vacancy to form Li antisites. Similar reactions may take place for Al antisites. The term $\dot{g}_{ij}^{ex}$ added to $\dot{g}_d^R$ describes these reactions. The rates of these reactions depend on the bonding energy $E_{Ai\_BV}^b$ between interstitial and vacancy. $E_{Li\_AlV}^b$ and $E_{Al\_LiV}^b$ are -7.15eV and -9.30eV, respectively [21], indicating that Al antisite is energetically favored. In addition, the defects in $LiAlO_2$ are charged. For instance, Li and Al interstitials have positive charges and their vacancies have negative charges. The O interstitial and O vacancy have negative and positive charges, respectively. Different charged defects may have strong interaction that affects the local chemical potentials. Density function theory (DFT) simulation shows that Al interstitial and O vacancy have strong binding energy (-3.5eV) [21]. The aggregation of charged defects causes an electric field that provides an additional diffusion driving force of defect diffusion. In this model, the long-range interaction between electric field and charged defects is ignored while the short-range interface between charged defects are indirectly described by the binding energies $E_{ij}^{binding}$ between defect *i* and *j* in Eq. (3). Most thermodynamic and kinetic properties required in the model are lacking although they can, in principle, be calculated using atomistic simulations. Therefore, in this work we conducted a parametric study to assess the effect of thermodynamic and kinetic properties on RIS in $LiAlO_2$, and demonstrate the capability of the developed model. In the following simulations, we used a polycrystalline structure with a simulation cell $256l_0 \times 256l_0 \times 1l_0$ in two dimensions.

4.3 Effect of Li chemical potential on segregation in $LiAlO_2$

For a given chemical potential of Al and O on grain boundaries $\mu_{Al}^{GB} = 0eV$ and $\mu_O^{GB} = 0eV$, the effect of Li chemical potentials ($\mu_{Li}^{GB} = -0.1eV, -0.5eV,$ and $-1.0eV$) on RIS were simulated. For $\mu_{Li}^{GB} = -0.5eV$ the evolution of Al, Li, and O concentration changes and total vacancy concentrations are shown in Fig. 5. The results clearly indicate that as time increases: 1) the

depletion of Al and O on grain boundaries increases and the segregation of Al and O at the center of grains increases, 2) the segregation of Li on grain boundaries increases, and 3) total vacancy concentration including Li, Al, and O vacancies depends on grain sizes. To compare the effect of μ_{Li}^{GB} on RIS, the distribution of concentration changes on the line BB' in Fig. 1(a) at $t = 51401s$ are plotted in Fig. 6. As the chemical potential μ_{Li}^{GB} decreases, Li segregation on grain boundaries increases, the segregation of Al and vacancies inside grains increases, and O segregation inside grains slightly decreases. Checking O vacancy concentration, one finds that O vacancy segregates on grain boundaries and increases with the decrease of μ_{Li}^{GB}. The result indicates that O has a flux from grain boundary to inside the grain, while O vacancy has a flux from inside grains to grain boundaries. The low total vacancy concentration inside larger grains shown in Fig. 5(c) also demonstrates that the vacancy flux is dominated by O vacancies.

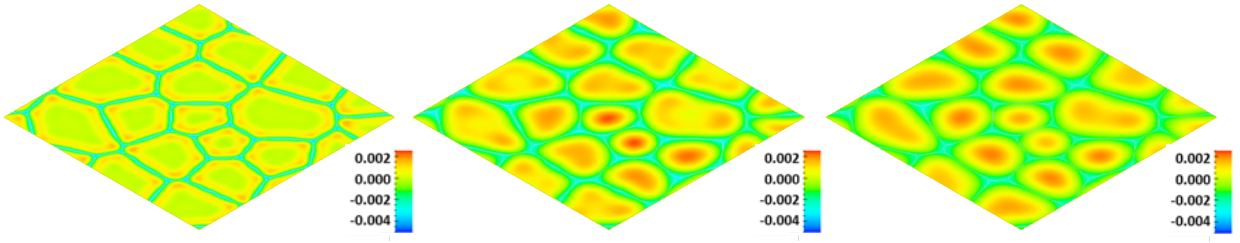

Change of Al concentration at [Al, Li] sublattice

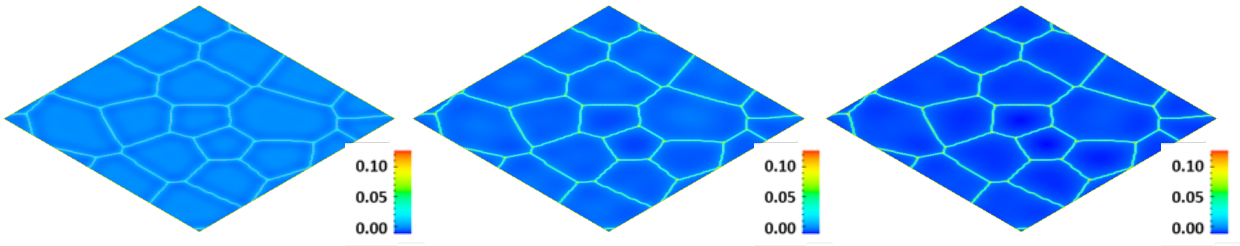

Change of Li concentration at [Al, Li] sublattice

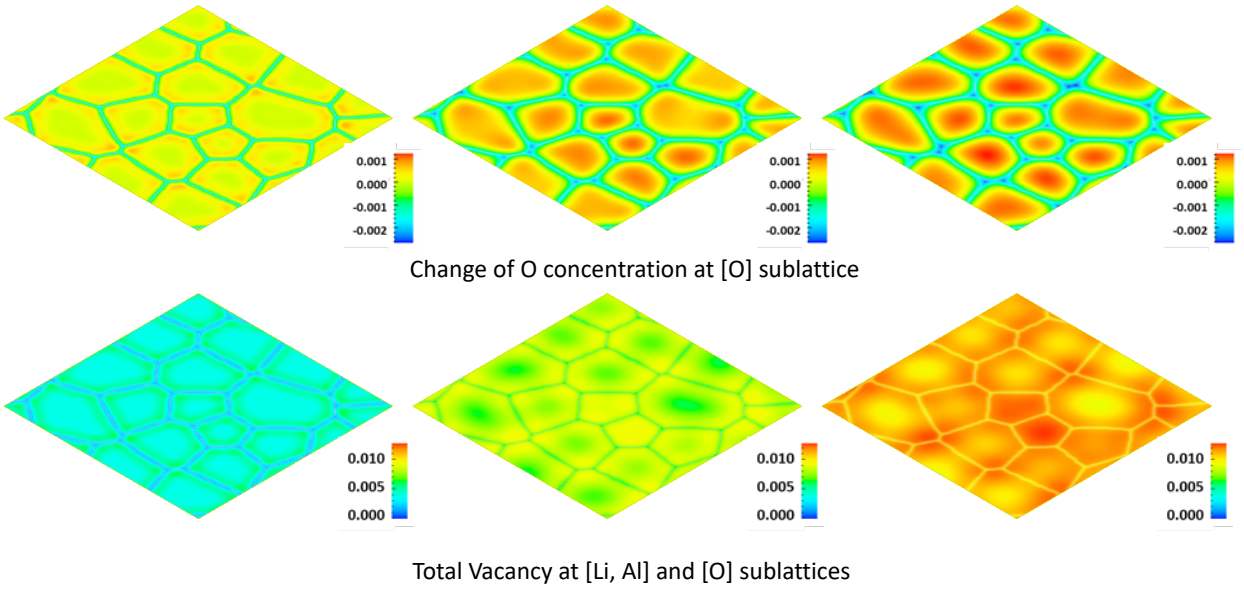

Fig. 5. Evolution of Al, Li, and O concentration changes and total vacancy concentration for Li chemical potential on grain boundaries $\mu_{Li}^{GB} = -1.0eV$ at (a) $t^* = 56$, (b) $t^* = 945$, and (c) $t^* = 2056$.

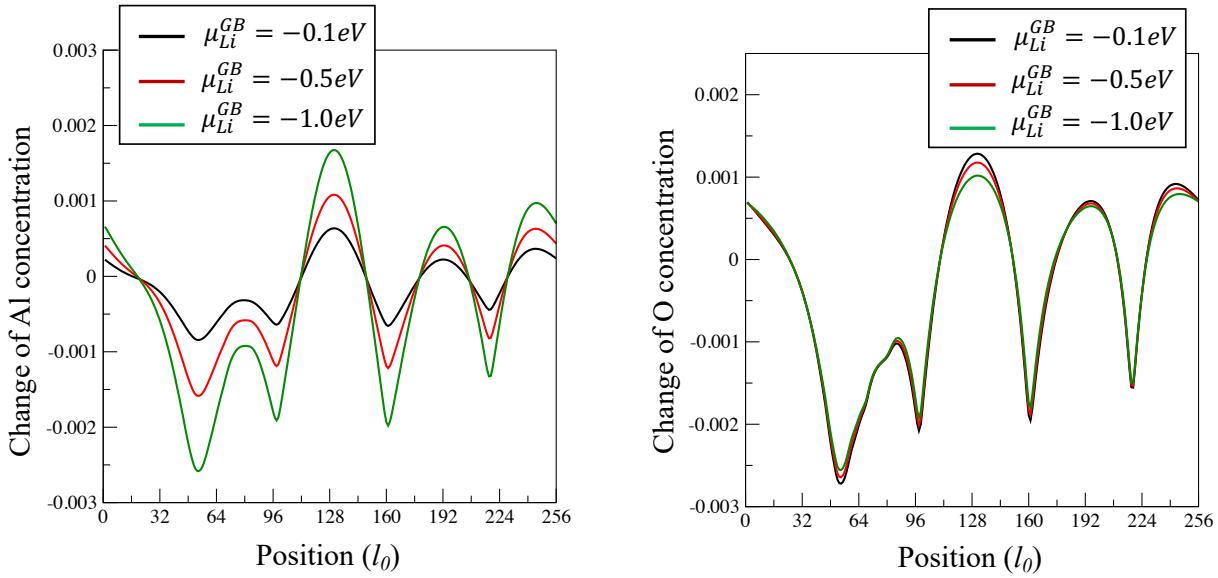

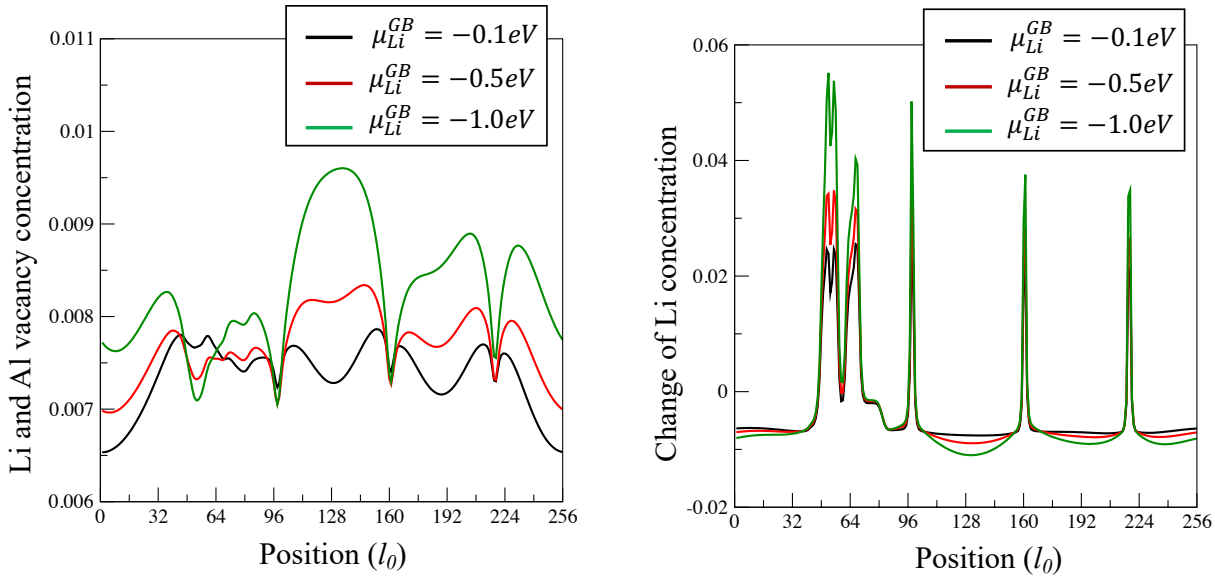

Fig. 6. Comparison of Li, Al, O and vacancy concentration distributions along BB' in Fig. 1(a) at $t^* = 2056$ for different chemical potential of Li on grain boundaries.

Because grain boundaries are sinks of Li with $S_0 = 0.2$, the change of total Li concentration at grain boundaries or Li release from the grain boundaries can be calculated by

$$\Delta\bar{c}_{Li} = \iint_S \left\{ \int_0^t \dot{S}_i \, dt \right\} d\, A/A_0 \tag{25}$$

where A_0 is the area of grain boundaries. Fig. 7 shows that Li release increases with the decrease of the chemical potential μ_{Li}^{GB}.

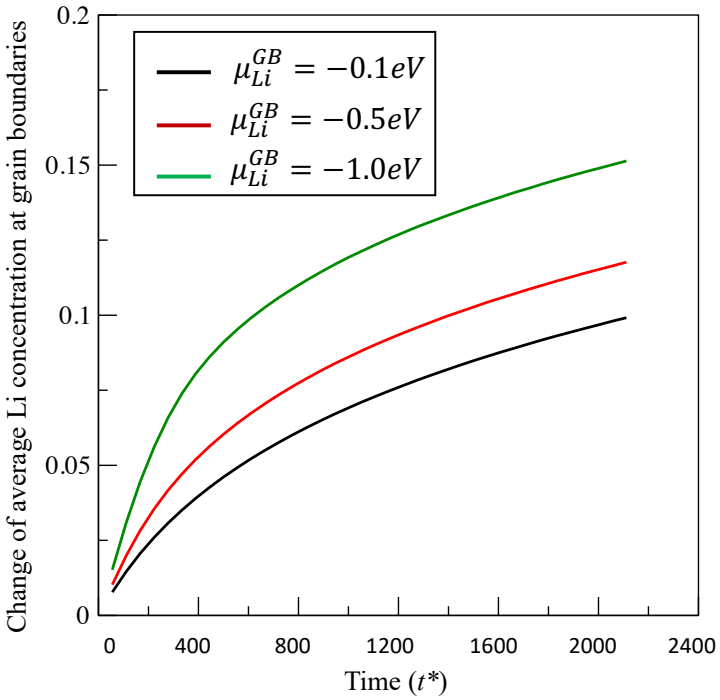

Fig. 7. Average Li release from grain boundaries in terms of Li chemical potential μ_{Li}^{GB}.

4.4 Effect of Li interstitial and Al vacancy bonding energy on segregation in $LiAlO_2$

MD simulations show that high-energy cascades generate a large amount of antisite defects at the [Li, Al] sublattice. The binding energy between interstitial and vacancy determines the antisite stability. DFT results show that Al antisite has much lower energy than Li antisite [21]. It is expected that Al interstitials are energetically favored to form Al antisites or Li antisites are more likely to associate to Li interstitials and Al vacancies than Al antisites. The exchange rate $\dot{g}_{ij}^{ex}$ describes these reactions. The effect of exchange rate between Li interstitial and Al vacancy on concentration in RIS are shown in Fig. 8. Varying the coefficient β_{ij} of the exchange rate $\dot{g}_{ij}^{ex}$ from -0.25 to 0.25 means the easier formation of Li antisites to the easier association of Li antisite. The association of Li antisites results in more mobile Li interstitials while the formation of Li antisite results in less mobile Li interstitials. As expected, the results in Fig. 8 show that the Li release from grain boundaries increases with the increase of the exchange rate $\dot{g}_{ij}^{ex}$ (i.e., the association of Li antisites).

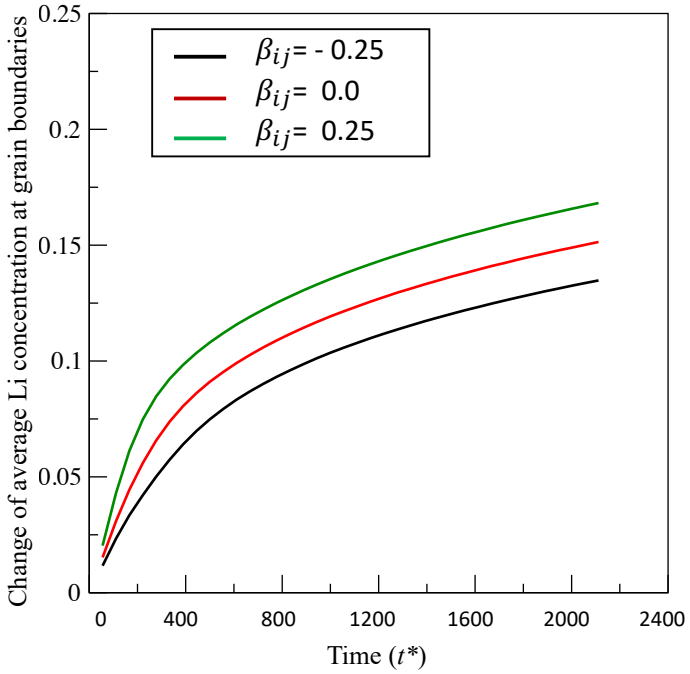

Fig. 8. Effect of formation and association of Li antisites on RIS.

4.5 Effect of interstitial diffusivity on segregation in $LiAlO_2$

Defect mobility is one of most important properties that affects the direction of solute diffusion, hence, the segregation and/or depletion of solutes. Fig. 9 plots the effect of the ratio of Al interstitial and Li interstitial diffusivity on RIS. It can be seen that for a given d_{Ai} as d_{Bi} increases from $0.001d_{Ai}$ to d_{Ai} the average Li release from grain boundaries first increases, then decreases. For different d_{Bi}/d_{Ai}, vacancy concentration distributions on the line BB' are plotted in Fig. 10. When d_{Bi}/d_{Ai} is small, vacancies on both Li and Al sublattice and O sublattice accumulate on grain boundaries. With the increase of d_{Bi}/d_{Ai}, vacancy segregation on grain boundaries gradually becomes depleted, and the total vacancy concentration decreases. The results indicate that a slow Al interstitial diffusivity increases vacancy concentration in the matrix and results in a fast Li release. Examining the Li, Al, and O concentration evolution, it is found that the Al interstitial diffusivity d_{Bi} changing from $0.001d_{Ai}$ to d_{Ai} does not affect their segregation and depletion tendencies on grain boundaries. However, the segregation of Li and the depletion of Al and O on grain boundaries increase with the decrease of Al interstitial diffusivity d_{Bi} for a given Li interstitial diffusivity d_{Ai}.

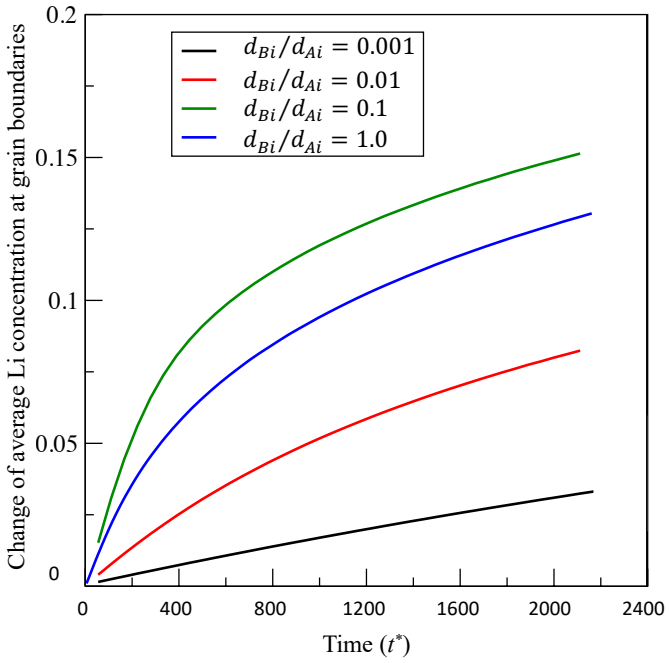

Fig. 9. Effect of the ratio between Al and Li interstitial diffusivity on Li segregation on grain boundaries.

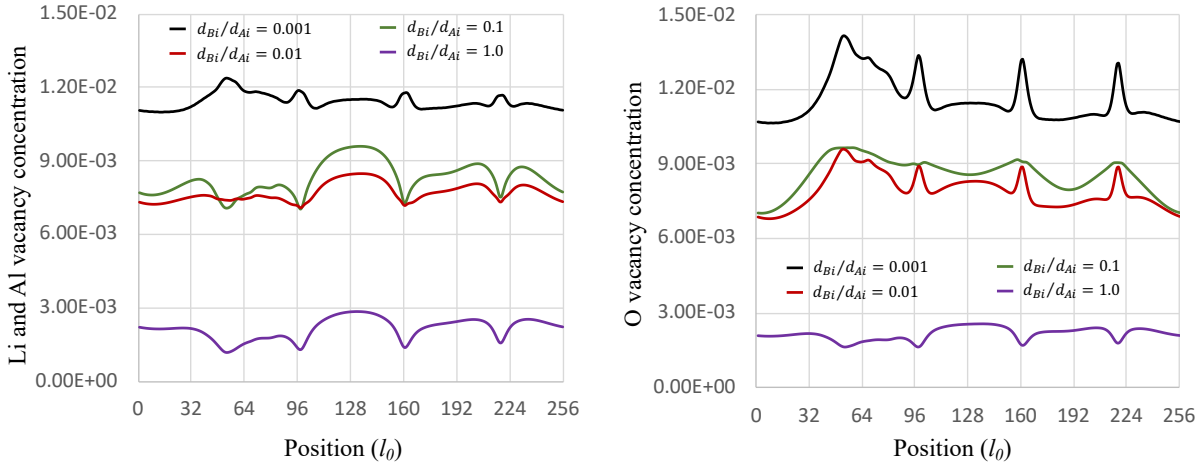

Fig. 10. Effect of the ratio between Al and Li interstitial diffusivity on vacancy distribution on the line BB' from Fig. 1(a) at $t^* = 2000$.

4.6 Effect of Al and O interstitial binding energy on segregation in $LiAlO_2$

Al interstitial and O interstitial may have a strong interaction because they have opposite charges, which is measured by $E_{ij}^{binding}$. This binding energy either results in a concentration dependence of chemical potentials as described in Eq. (3), or a concentration dependence of diffusivity as described in the rate theory [8]. In this section, we simulated the effect of a concentration dependence of chemical potentials on RIS. The results in Fig. 11 show that attracting interaction ($E_{ij}^{binding} < 0$) between Al and O interstitial reduces the Li release from grain boundaries while a repelling interaction ($E_{ij}^{binding} > 0$) increases the Li release from grain boundaries. From Eq. (3) if $E_{ij}^{binding} < 0$, the chemical potential of Al interstitial will be proportional to $c_{oi}E_{ij}^{binding}$, and the interaction between Al and O interstitials provide a driving force that is proportional to -$E_{ij}^{binding}\nabla c_{oi}$. As a result, Al interstitial has an additional flux in the direction parallel to ∇c_{oi}. Fig. 12 plots the distributions of Al and O interstitials, and vacancies at Al and Li sublattice along the line BB'. The results show that O interstitial segregates inside the grain. This means that the direction of O interstitial gradient ∇c_{oi} points to the center of grains. So Al should have an additional flux to the center of grains. The result in Fig. 12(a) confirms that Al interstitial at the center of grains has a higher concentration when $E_{ij}^{binding} < 0$ and a lower concentration when $E_{ij}^{binding} > 0$ compared with that when $E_{ij}^{binding} = 0$. $E_{ij}^{binding}$ has an opposite effect on vacancies at Li and Al sublattice. A negative $E_{ij}^{binding}$ reduces the vacancy concentration at the center of grains. The decease of Li release with the increase of $E_{ij}^{binding}$ may be attributed to the decrease of vacancy concentration in the matrix as observed in Section 4.4.

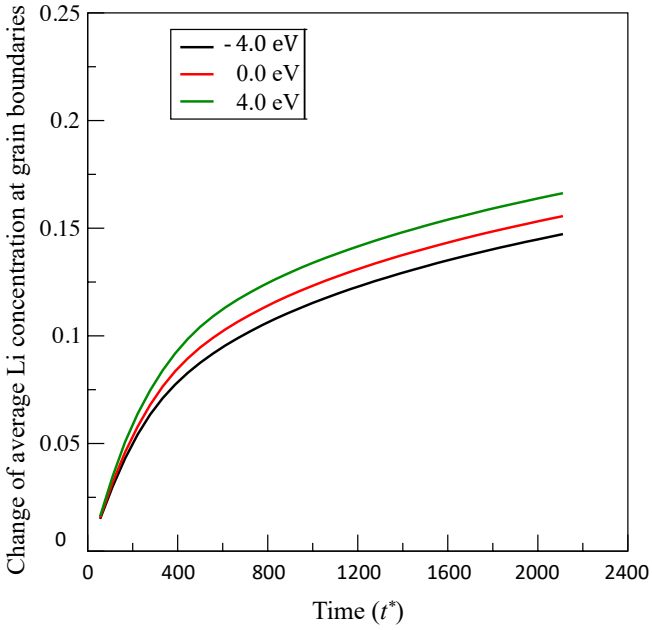

Fig. 11. Effect of the binding energy between Al and O interstitials on Li segregation on grain boundaries.

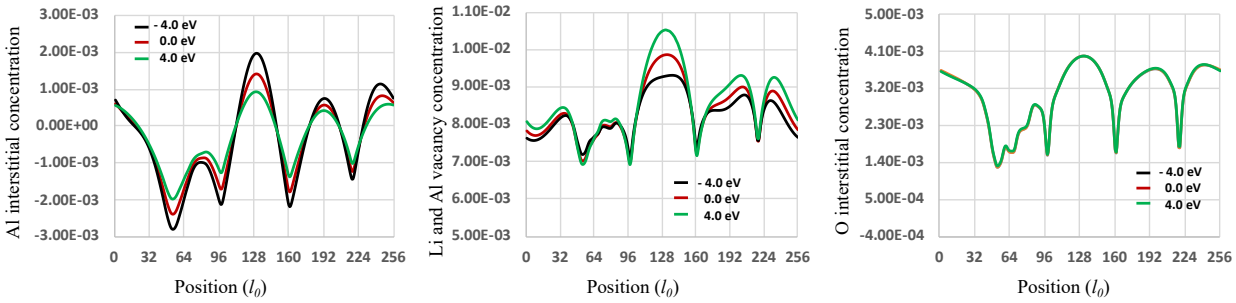

Fig. 12. Effect of the binding energy on Al interstitial and O interstitial, Vacancy at Li and Al sublattice and O interstitial distribution on the line BB' from Fig. 1(a) at $t^* = 2000$.

5.0 Conclusions and Discussion

A microstructure-dependent rate theory model has been developed to investigate RIS in polycrystalline $LiAlO_2$. The model assumed that the defect migration is driven by chemical potential gradient. All the thermodynamic and kinetic properties of defects including chemical potentials, diffusivities, sink strengths, and reaction rates are described as being microstructure-

dependent by a set of phase-field order parameters that represent the grain orientations. In binary alloys, the predicted effect of relative defect mobility (inverse Kirkendall effect) on RIS is in agreement with rate theory. The results also show that the chemical potential of solutes on grain boundaries, which is ignored in the conventional rate theory, plays an important role on RIS as the relative diffusivity of defects and solutes. DFT and MD simulations demonstrated that the defect configuration in irradiated $LiAlO_2$ are very complicated due to a potential charge effect. In the current model, all the defects are treated as electrical neutral. In addition, since most thermodynamic and kinetic properties of defects are lacking in $LiAlO_2$, a parametric study of the effect of defect thermodynamic and kinetic properties on RIS was carried out with the developed model. The results indicate that for the case when Li has a lower chemical potential (thus strong sinking strength on grain boundaries) and a higher mobility than Al and O, Li tends to segregate on grain boundaries while Al and O tend to segregate at the center of grains. With the knowledge of phase diagram in Li_2O and Al_2O_3 system [39], the enrichment of Li on grain boundaries may result in the dissolution of $LiAl_5O_8$. The enrichment of Al and O at the centers of grains may cause the formation of $LiAl_5O_8$. Such dissolution and formation of $LiAl_5O_8$ particles are observed in irradiated $LiAlO_2$. Energy-particle cascades generate a large portion of antisite defects such as Li_{Al} and Al_{Li} [4]. DFT calculations showed a large difference for the formation of antisite defects (Li_{Al}, Al_{Li}, Al_O). It is found that the dissociation of Li_{Al} increases the Li segregation on grain boundaries and Li release from grain boundaries. The ratio of Al interstitial and Li interstitial diffusivity significantly affects Li segregation on grain boundaries. Also, given d_{Ai} (A=Li) while d_{Bi} (B=Al) increases from $0.001d_{Ai}$ to d_{Ai}, the average Li release from grain boundaries first increases then decreases. For example, the interaction between charged defects Al interstitial and O interstitial with opposite charges, has been indirectly described by concentration-dependent chemical potentials with their binding energy. The results showed that an attracting interaction ($E_{ij}^{binding} < 0$) between Al and O interstitial reduces Li segregation on grain boundaries while a repelling interaction ($E_{ij}^{binding} > 0$) increases the Li segregation.

In summary, the simulations demonstrate the model capability for assessing the effect of thermodynamic and kinetic properties of defects on the segregation or depletion of species in polycrystalline $LiAlO_2$, and for predicting the effect of irradiation conditions on phase stability. The defect evolution is important for studying the microstructure evolution of $LiAl_5O_8$ and voids

in irradiated $LiAlO_2$ that are key for predicting the material degradation such as thermal conductivity and for modeling the effect of microstructures on tritium release kinetics. Although the model has the capability, the results are qualitative because of the lack of thermodynamic and kinetic properties such as the chemical potential of species on grain boundaries, the binding energies of different defects, and the diffusivities of mobile defects. Lee et al. [21] calculated the formation energies of defects in a single crystal LiAlO2. The follow-on work of this team will inform the thermodynamic and kinetic properties of defects for the model presented in this work. Furthermore, all the defects in $LiAlO_2$ are charged. The accumulation or depletion of defects might cause an electric field that affects the thermodynamic and kinetic properties of defects. For follow-on work we will modify the model by taking the charge and electric interaction into account.

Acknowledgment

This research was supported by the National Nuclear Security Administration of the U.S. Department of Energy through the Tritium Technology Program at Pacific Northwest National Laboratory. Computation was performed using Environmental Molecular Sciences Laboratory (EMSL) computing resources at Pacific Northwest National Laboratory.

References

[1] E.C. Buck, D.D. Reilly, P.J. MacFarlan, B.W. Arey, J.A. TRevino, G.J. Sevigny, Irradiated Tritium-Bearing Pellet Characterization, DOE technical report PNNL-28289 (2018).

[2] D.J. Senor, Recommendations for Tritium Science and Technology Research and Development in Support of the Tritium Readiness Campaign, DOE technical report PNNL-27216 (2017).

[3] D.E. Burkes, D.J. Senor, G. Longoni, J.M. Johns, Roadmap to Establish an Integrated TPBAR Performance Model, Pacific Northwest National Laboratory PNNL-SA-121864(presented at Tritium Focus Group, Rochester, NY, October 25, 2016) (2016).

[4] W. Setyawan, D.J. Senor, R. Devanathan, Insights on amorphization of lithium aluminate from atomistic simulation, Journal of Physical Chemistry C 121(14) (2017) 7635-7642.

[5] H. Wiedersich, P.R. Okamoto, N.Q. Lam, Theory of radiation-induced segregation in concentrated alloys, Journal of Nuclear Materials 83(1) (1979) 98-108.

[6] S.I. Golubov, A.M. Ovcharenko, A.V. Barashev, B.N. Singh, Grouping method for the approximate solution of a kinetic equation describing the evolution of point-defect clusters, Philosophical Magazine a-Physics of Condensed Matter Structure Defects and Mechanical Properties 81(3) (2001) 643-658.

[7] G.S. Was, T.R. Allen, J.T. Busby, J. Gan, D. Damcott, D. Carter, M. Atzmon, E.A. Kenik, Microchemistry and microstructure of proton-irradiated austenitic alloys: toward an understanding of irradiation effects in LWR core components, Journal of Nuclear Materials 270(1-2) (1999) 96-114.

[8] G. Was, Fundamentals of Radiation Materials Science: Metals and Alloys, New York: Springer, 2007.

[9] A.D. Brailsford, R. Bullough, The Theory of Sink Strengths, Philosophical Transactions of the Royal Society a-Mathematical Physical and Engineering Sciences 302(1465) (1981) 87-137.

[10] D. Brimbal, L. Fournier, A. Barbu, Cluster dynamics modeling of the effect of high dose irradiation and helium on the microstructure of austenitic stainless steels, Journal of Nuclear Materials 468 (2016) 124-139.

[11] T. Faney, B.D. Wirth, Spatially dependent cluster dynamics modeling of microstructure evolution in low energy helium irradiated tungsten, Modelling and Simulation in Materials Science and Engineering 22(6) (2014).

[12] J.H. Ke, H.B. Ke, G.R. Odette, D. Morgan, Cluster dynamics modeling of Mn-Ni-Si precipitates in ferritic-martensitic steel under irradiation, Journal of Nuclear Materials 498 (2018) 83-88.

[13] D.H. Xu, B.D. Wirth, Spatially Dependent Rate Theory Modeling of Thermal Desorption Spectrometry of Helium-Implanted Iron, Fusion Science and Technology 56(2) (2009) 1064-1068.

[14] D.H. Xu, B.D. Wirth, Modeling spatially dependent kinetics of helium desorption in BCC iron following He ion implantation, Journal of Nuclear Materials 403(1-3) (2010) 184-190.

[15] Y.L. Li, S.Y. Hu, X. Sun, M. Stan, A review: applications of the phase field method in predicting microstructure and property evolution of irradiated nuclear materials, Npj Comput Mater 3 (2017).

[16] J.D. Hales, M.R. Tonks, F.N. Gleicher, B.W. Spencer, S.R. Novascone, R.L. Williamson, G. Pastore, D.M. Perez, Advanced multiphysics coupling for LWR fuel performance analysis, Annals of Nuclear Energy 84 (2015) 98-110.

[17] S. Rokkam, A. El-Azab, P. Millett, D. Wolf, Phase field modeling of void nucleation and growth in irradiated metals, Model. Simul. Mater. Sci. Eng. 17(6) (2009) 064002.

[18] M.R. Tonks, A. Cheniour, L. Aagesen, How to apply the phase field method to model radiation damage, Computational Materials Science 147 (2018) 353-362.

[19] L.D. Xia, Y.Z. Ji, W.B. Liu, H. Chen, Z.G. Yang, C. Zhang, L.Q. Chen, Radiation induced grain boundary segregation in ferritic/martensitic steels, Nuclear Engineering and Technology 52(1) (2020) 148-154.

[20] S. Hu, Y. Li, D. Burkes, D.J. Senor, Microstructure-Dependent Rate Theory Model of Radiation-Induced Segregation in Binary Alloys, Frontiers in Materials 8(170) (2021) 682686.

[21] Y.L. Lee, J. Holber, H.P. Paudel, D.C. Sorescu, D.J. Senor, Y.H. Duan, Density functional theory study of the point defect energetics in gamma-LiAlO2, Li2ZrO3 and Li2TiO3 materials, Journal of Nuclear Materials 511 (2018) 375-389.

[22] H.L.F.S.G.S.B. Lukas, Computational thermodynamics : the CALPHAD method, (2007).

[23] Z.-k. Liu, Y. Wang, Computational Thermodynamics of Materials, 2016.

[24] J.D. van der Waals, The Thermodynamic Theory of Capillarity under the Hypothesis of a Continuous Variation of Density, Journal of Statistical Physics 20(2) (1979) 200-244.

[25] R.D. Kamachali, A.K. da Silva, E. McEniry, D. Ponge, B. Gault, J. Neugebauer, D. Raabe, Segregation–Assisted Spinodal and Transient Spinodal Phase Separation at Grain Boundaries, https://arxiv.org/abs/1905.07970 (2019).

[26] J.B. Piochaud, M. Nastar, F. Soisson, L. Thuinet, A. Legris, Atomic-based phase-field method for the modeling of radiation induced segregation in Fe-Cr, Computational Materials Science 122 (2016) 249-262.

[27] L. Onsager, Reciprocal relations in irreversible processes. I., Physical Review 37(4) (1931) 405-426.

[28] J.P. Wharry, G.S. Was, The mechanism of radiation-induced segregation in ferritic-martensitic alloys, Acta Materialia 65 (2014) 42-55.

[29] T.S. Duh, J.J. Kai, F.R. Chen, L.H. Wang, Numerical simulation modeling on the effects of grain boundary misorientation on radiation-induced solute segregation in 304 austenitic stainless steels, Journal of Nuclear Materials 294(3) (2001) 267-273.

[30] V. Kuksenko, C. Pareige, P. Pareige, Intra granular precipitation and grain boundary segregation under neutron irradiation in a low purity Fe–Cr based alloy, Journal of Nuclear Materials 425(1) (2012) 125-129.

[31] H. Zhao, F. De Geuser, A. Kwiatkowski da Silva, A. Szczepaniak, B. Gault, D. Ponge, D. Raabe, Segregation assisted grain boundary precipitation in a model Al-Zn-Mg-Cu alloy, Acta Materialia 156 (2018) 318-329.

[32] L.R. Greenwood, Radiation damage calculations for the FUBR and BERTRIX irradiations of lithium compounds in EBR41 and FFTF, Fusion materials semiannual progress report for period ending, 1999, pp. 187-193.

[33] M.M. Islam, T. Bredow, Interstitial Lithium Diffusion Pathways in gamma-LiAlO2: A Computational Study, Journal of Physical Chemistry Letters 6(22) (2015) 4622-4626.

[34] D. Wiedemann, S. Nakhal, J. Rahn, E. Witt, M.M. Islam, S. Zander, P. Heitjans, H. Schmidt, T. Bredow, M. Wilkening, M. Lerch, Unravelling Ultraslow Lithium-Ion Diffusion in gamma-LiAlO2: Experiments with Tracers, Neutrons, and Charge Carriers, Chemistry of Materials 28(3) (2016) 915-924.

[35] J.P. Jacobs, M.A. SanMiguel, L.J. Alvarez, P.B. Giral, Lithium diffusion in gamma-LiAlO2, a molecular dynamics simulation, Journal of Nuclear Materials 232(2-3) (1996) 131-137.

[36] Q.W. Hu, L. Lei, X.D. Jiang, Z.C. Feng, M.J. Tang, D.W. He, Li ion diffusion in LiAlO2 investigated by Raman spectroscopy, Solid State Sciences 37 (2014) 103-107.

[37] S. Indris, P. Heitjans, R. Uecker, B. Roling, Li Ion Dynamics in a LiAlO2 Single Crystal Studied by Li-7 NMR Spectroscopy and Conductivity Measurements, Journal of Physical Chemistry C 116(27) (2012) 14243-14247.

[38] D. Wohlmuth, V. Epp, P. Bottke, I. Hanzu, B. Bitschnau, I. Letofsky-Papst, M. Kriechbaum, H. Amenitsch, F. Hofer, M. Wilkening, Order vs. disorder-a huge increase in ionic conductivity of nanocrystalline LiAlO2 embedded in an amorphous-like matrix of lithium aluminate, Journal of Materials Chemistry A 2(47) (2014) 20295-20306.

[39] N.S. Kulkarni, T.M. Besmann, K.E. Spear, Thermodynamic Optimization of Lithia-Alumina, Journal of the American Ceramic Society 91(12) (2008) 4074-4083.